ISSN (Print) 1226-1750
ISSN (Online) 2233-6656
Journal of Magnetics 23(2), 253-266 (2018) https://doi.org/10.4283/JMAG.2018.23.2.253

Analytical Modelling of Open-Circuit Flux Linkage, Cogging Torque and Electromagnetic Torque for Design of Switched Flux Permanent Magnet Machine

Noman Ullah[1,2]*, Faisal Khan[1], Wasiq Ullah[1], Abdul Basit[2], Muhammad Umair[1], and Zeeshan Khattak[1]

[1]*Department of Electrical Engineering, COMSATS Institute of Information Technology, Abbottabad, Pakistan*
[2]*U.S.-Pakistan Center for Advanced Studies in Energy, University of Engineering & Technology, Peshawar, Pakistan*

(Received 14 February 2018, Received in final form 31 May 2018, Accepted 31 May 2018)

Magnetic saturation and complex stator structure of Switched Flux Permanent Magnet Machine (SFPMM) compels designers to adopt universally accepted numerical method of analysis i.e. Finite Element Analysis (FEA). FEA is not preferred for initial design due to its computational complexity and is time consuming process because of repeated iterations. This paper presents an accurate analytical approach for initial design of proposed twelve-stator-slot and ten-rotor-tooth (12/10) with trapezoidal slot structure SFPMM. Air-gap Magnetic Equivalent Circuit (MEC) models with Global Reluctance Network (GRN) methodology is utilized for calculation of open-circuit flux linkage. Fourier Analysis (FA) for cogging torque, and Maxwell Stress Tensor (MST) method for electromagnetic torque where radial and tangential components of the air-gap flux density are produced by the currents flowing in three phase armature winding. Analytical predictions are validated by FEA utilizing JMAG software and shows errors less than ~2% for open-circuit flux linkage, ~4.2% for cogging torque, and ~2% for average electromagnetic torque.

Keywords : Switched Flux Permanent Magnet Machine, Fourier Analysis, Maxwell Stress Tensor Method, Analytical Modelling, Magnetic Equivalent Circuit Models, Global Reluctance Network Methodology

1. Introduction

Switched Flux Permanent Magnet Machine (SFPMM) combines unique features of Permanent Magnet Synchronous Machines (PMSM) i.e. high torque and power density, and Switched Reluctance Machines (SRM) i.e. robust rotor structure by placing both Permanent Magnet (PM) and armature winding on primary (stator) of machine leaving secondary (rotor) completely passive. Passive rotor without any winding or PM enables; robust rotor structure, makes this machine suitable for applications where ruggedness and high speed is concerned, can be used in electric vehicle traction, aerospace, and wind applications due to its compatibility with extreme environmental conditions [1-4]. SFPMM was introduced in 1955 as generator [5] by placing permanent magnet having opposite polarities between two consecutive stator slots.

SFPMM received attention of designers in the recent past, about two decades and a lot of research is carried out in this field. Design and structure of SFPMM resembles with doubly salient permanent magnet machine [6, 7] having additional advantages of: (a) favorable for cooling due to the location of magnets in the stator especially for applications where ambient temperature is relatively high, e.g. electric locomotives [8, 9], (b) SFPMM makes it possible for the armature windings to remagnetize the magnets by changing the winding connections appropriately when the magnets performance are degraded, (c) bipolar flux linkage, (d) easy flux weakening operation at high speed [10], (e) compared to conventional fractional-slot PM machine, slot area of SFPMM is reduced due to PM and armature winding being on the stator, but flux focusing is utilized, and high electromagnetic performance can be achieved [11], (f) SFPMM has sinusoidal back-EMF, and (g) similar to SRM, SFPMM has no PMs, armature windings, or brushes on the rotor, thus offering good mechanical integrity and high reliability for high speed operation.

Limitation about SFPMM is cost of rare earth PM material and a sophisticated computer aided design. Complex stator structure (due to presence of both PMs and armature windings) and magnetic saturation of SFPMM

©The Korean Magnetics Society. All rights reserved.
*Corresponding author: Tel: +92-33-656-42442
Fax: +92-0992-383441, e-mail: nomanullah@ciit.net.pk

© 2018 Journal of Magnetics

compels designers to adopt universally accepted numerical method of analysis i.e. Finite Element Analysis (FEA). FEA is widely used in performance analysis [12-14] and optimization design [15] of electric machines, since it can precisely obtain the flux density distribution [16]. However, it is time-consuming, especially in trade-off designs of electrical machines [17]. FEA techniques are arduous and iterative offline methods. Moreover, multiphase machines are still often obtained rewinding stators of conventional three phase machines, which means that the resulting machine is not optimal, and the electrical parameters are difficult to obtain using FEA or similar computational techniques [18]. Furthermore, FEA consider geometric details and non-linearity of magnetic materials for electromagnetic field analysis, Since they require expensive software/hardware, large computational time, large computer memory, and large disk storage due to repeated iterations [19].

Consequently, analytical techniques are developed to analyze and optimize electric machines regarding different parameters such as; authors in [20] examined optimal stator and rotor pole combinations regarding Back Electromotive Force (B-EMF). Stator Mounted Permanent Magnet Machines (SMPMM) can be divided into: Doubly Salient Permanent Magnet Machines (DSPMM), Switched Flux Permanent Magnet Machines (SFPMM), and Flux Reversal Permanent Magnet Machines (FRPMM). SFPMM has additional advantages of: low copper loss [21], high power density [22], and high efficiency [23] as compared to other two topologies. Comparative study of FRPM machines and SFPMM is done based on general power equations in [24]. Analytical torque equations for SFPMM and Interior Permanent Magnet (IPM) machines are developed in [25] and revealed that electromagnetic performance of the SFPMM machine is similar to, or even better than, that of the IPM machine.

An analytical approach for air-gap modeling of ten-stator-slot and eight-rotor-tooth Field-Excited Flux Switching Machine (FEFSM) is developed in [26] and discussed flux linkage, Back-EMF, and Unbalanced Magnetic Forces (UMF). Authors of [27] discussed variable MEC methodology for in-wheel motor used in Electric Vehicles (EVs) by accounting three motors having different dimensions. Furthermore, 3-D lumped-parameter magnetic circuit model in [28] is developed for a single-phase flux-switching permanent-magnet motor representing complex air-gap flux paths by equivalent permeances. In [29], authors explains that calculation time of nonlinear MEC for Surface mounted PM (SPM) machines which takes iron saturation effect into account, was approximately 1/1280 to that of FEA. Meshing of geometry is involved in MEC methodology, however number of elements and nodes are in acceptable limits and can be solved utilizing computational hardware/software. SFPMM can be designed with rectangular or trapezoidal slot structure that encloses armature winding.

FEA for trapezoidal slot structure machine require even more mathematical calculations due to its complex geometry [30]. Analytical modelling of open-circuit flux linkages utilizing MEC models for rectangular slot structure SFPMM is presented in [31]. While MEC models with GRN methodology for 12/10 trapezoidal slot structure SFPMM is presented in [32]. Double salient nature of SFPMM enables advantages of bipolar flux linkage, simple control strategy, and low cost. However, aforementioned property introduces a critical problem known as cogging torque, which ultimately results in torque ripples. FA provides accurate information about air-gap field distribution and can be utilized as initial design approach for SFPMM. However, FA does not include magnetic saturation [33] and speed of operation of machine affects its performance regarding computational time [34]. FA in combination with Maxwell force equation is used for magnetic noise reduction of induction motor in [35], FA is used to determine air-gap permeance function, then expression for air-gap flux density is developed and ultimately Maxwell force values resulting from all possible combinations of flux density are considered.

This paper contributes to analytical calculations of three fundamental parameters namely, (a) open-circuit flux linkage, (b) cogging torque, and (c) electromagnetic torque. MEC models of proposed twelve-stator-slot and ten-rotor-tooth (12/10) with trapezoidal slot structure SFPMM (as shown in Fig. 1, and fundamental parameters are described

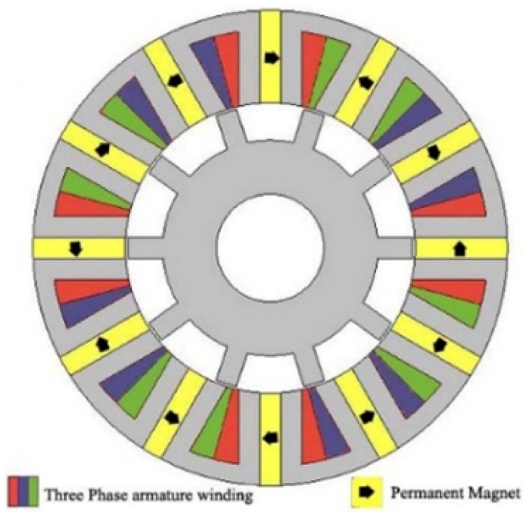

Fig. 1. (Color online) Cross section of 12/10 SFPMM.

Table 1. Dimensions and parameters of SFPMM.

Parameter (unit)	Symbol	Quantity
Stator outer radius (mm)	R_{so}	45
Stator slot depth (mm)	h_s	13.9
Stator back iron height (mm)	h_{si}	3.6
Stator inner radius (mm)	R_{si}	27.5
Rotor outer radius (mm)	R_{ro}	27
Rotor tooth height (mm)	h_{rt}	6.6
Rotor back iron height (mm)	h_{ri}	10.2
Air gap length (mm)	σ	0.5
Stack length (mm)	L	25
Rotor tooth width (mm)	R_{tw}	4
Stator slot width (mm)	S_{sw}	4
Rotor shaft radius (mm)	R_{sr}	10.2
PM relative Permeability	μ_r	1.05
PM remanence (T)	B_r	1.2
Rated Current (A)	I	5
Current density (A/mm^2)	J_a	30

in Table 1) corresponding to different rotor positions are combined as GRN and are solved utilizing incidence matrix methodology using MATLAB. Furthermore, energy method and FA technique of air-gap flux density and air-gap permeance is implemented to predict cogging torque of SFPMM. Moreover, MST method is integrated after prediction of both radial and tangential component of magnetic field, and ultimately electromagnetic torque is calculated for proposed SFPMM.

2. Analytical Modelling

Analytical modelling helps designers and researchers to analyze PM machines regarding: (a) optimal stator and rotor pole combinations, (b) optimal split ratio, (c) optimal slot opening, (d) optimal winding configurations, (e) open-circuit flux linkage, (f) cogging torque, (g) UMF, (h) electromagnetic torque, (i) B-EMF, and (j) self and mutual inductances. Major parameters such as flux linkage and air-gap permeances are directly influenced by rotor position due to double salient nature of SFPMM. In order to simplify modelling of SFPMM, following assumptions are made:

- Material assigned to core of stator and rotor have infinite permeability
- PMs are magnetized being in radial alignment
- Middle of rotor tooth aligned with middle of stator PM is assigned as position $\Theta = 0^o$
- All PMs have same magnetic properties and dimensions
- Flux leakage and end effect is negligible
- As SFPMM is rotary in nature and air-gap permeances repeats periodically, thus only half machine is modeled in this study.

2.1. Analytical prediction of open-circuit flux linkage

Stator of simulated SFPMM consists of twelve trapezoidal slot structures for armature winding and twelve PM slots with Neomax-35AH irreversible radial pattern. Stator winding is three-phase with alternate winding arrangement generating three-phase flux. PMs being in radial alignment have magnetization direction opposite to each other (Fig. 1). SFPMM rotor's structure has resemblance with rotor of SRM i.e. doubly salient rotor with no windings. This property give rise to an undesired sensitive relation of rotor position with air-gap magnetic flux distribution as shown in Fig. 2.

Reluctance networks of 12/10 SFPMM air-gap magnetic equivalent circuit modules corresponding to different rotor positions, rotor magnetic equivalent circuit modules and stator magnetic equivalent circuit modules are combined as Global Reluctance Network (GRN). Rotor magnetic equivalent circuit modules and stator magnetic equivalent circuit modules are considered as constant for all segments. Air-gap flux distribution mainly contribute to performance of SFPMM, as conversion of electrical machine energy takes place in this medium. MEC modules for air-gap vary with rotor position; this is known as position state shifting and each MEC modules repeats which suggest possibilities of reducing verities of GRN.

As the rotor position changes, air-gap flux paths or flux

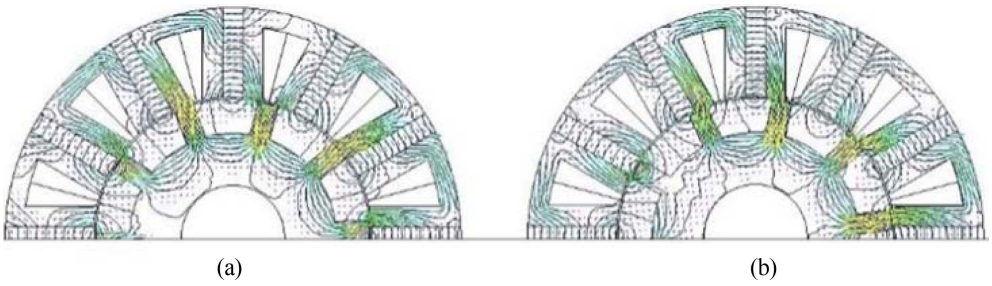

(a) (b)

Fig. 2. (Color online) Finite Element Analysis results of SFPMM at (a) Segment No. 1 and (b) Segment No. 2.

tubes changes resulting in changed flux tube permeance and also flux concentration. Area that encloses flux lines is defined as flux tubes [36]. To reduce errors and uplift accuracy of GRN, flux tubes permeance must be calculated accurately. Flux tubes for different rotor positions were analyzed based on position state shifting and concluded about periodic nature as these flux tubes are repeated, therefore half machine model is investigated. Various combinations of air-gap magnetic equivalent circuit modules corresponding to different rotor positions are implemented, variation of air-gap flux distribution is expressed as series of MEC modules and is termed as GRN.

2.1.1. Magnetic Equivalent Circuit Modules

Magnetic equivalent circuit consists of two categories of elements: passive elements as reluctances and active elements as sources. Active elements in magnet circuits are classified as; (a) Magnetomotive Force (mmf), and (b) flux sources. Regarding MEC, mmf sources are stator winding coils and Ampere's law is used for its mmf value calculations.

Figure 3(a) and Fig. 3(c) shows flux tubes having identical lengths of flux lines. Equation (1) is used to calculate total reluctance (R) of flux tube.

$$R = \int_0^{l_c} \frac{dx}{c(x)A(x)} \tag{1}$$

Where, $c(x)$ is material's properties, l_c is the length of flux tube and A is cross sectional area. Both A and $c(x)$ may vary through the length of flux tube.

Figure 3(b) and Fig. 3(d-f) shows flux tubes having different lengths of flux lines and identical cross-section

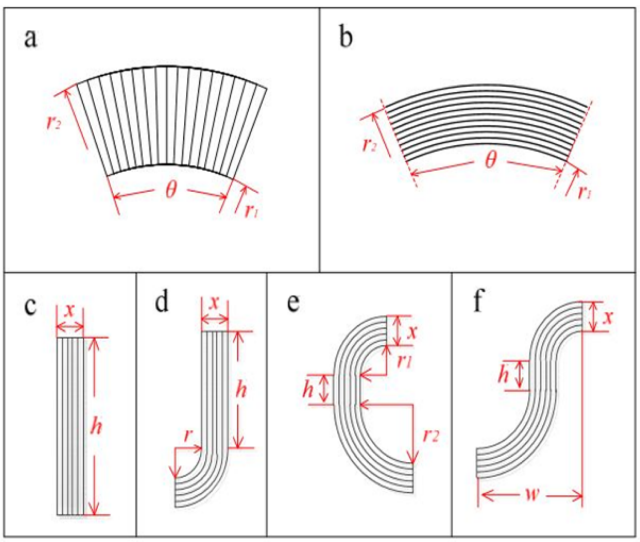

Fig. 3. (Color online) Cross sections of flux tubes.

Table 2. Flux tubes permeance (P) calculation formulas.

Flux tubes	Permeance (P)	Flux tubes	Permeance (P)
a	$\frac{\mu L\theta}{\ln\left(\frac{r_2}{r_1}\right)}$	d	$\frac{2\mu L.\ln\left(1+\frac{\pi x}{\pi r+2h}\right)}{\pi}$
b	$\frac{\mu L\ln\left(\frac{r_2}{r_1}\right)}{\theta}$	e	$\frac{\mu L.\ln\left(1+\frac{2\pi x}{\pi r_1+\pi r_2+2h}\right)}{\pi}$
c	$\frac{\mu Lx}{h}$	f	$\frac{2\mu Lx}{(\pi w+2h)}$

faces. Equation (2) is used to calculate total permeance (P) of flux tube.

$$P = \iint \frac{c(A)}{l_c} dA \tag{2}$$

Where, $c(A)$ is material's properties, l_c is the length of flux tubes, and A is cross sectional area. Both l_c and $c(A)$ vary over area A.

Six different flux tubes are evaluated in this paper (as shown in Fig. 3(a-f)) and their respective permeance (P) calculation formulas are shown in Table 2 [36]. X-axis of flux tubes show flux paths (equally distributed lines) and Y-axis represents magnetic properties of each flux path (assumed to be homogenous). Fig. 3(a) and Fig. 3(b) shows two types of flux tubes and their permeance calculations are done using cylindrical coordinate system to reduce computational complexity while Fig. 3(c-f) flux tubes permeance calculations are done using Cartesian coordinate system [36].

2.1.1.1. Permanent Magnet MEC Modules

PM is an active element, acts as a source and can be modeled as: (a) flux sources with permeance/reluctance in parallel, or (b) mmf source with permeance/reluctance in series. Equation (3) and (4) are used to calculate $\mathcal{F}_{PM}$ (mmf source) and Φ_{PM} (flux source).

$$\mathcal{F}_{PM} = \frac{B_r.l_{PM}}{\mu_0\mu_r} \tag{3}$$

$$\Phi_{PM} = B_r.A_{PM} \tag{4}$$

Where, B_r is remanent magnetic flux density of PM, l_{PM} is length of PM in magnetization direction, μ_r is relative permeability of PM, and A_{PM} is the cross-sectional area of PM. Permeance and reluctance can be calculated using approximations in simplifying the flux paths into different flux tubes.

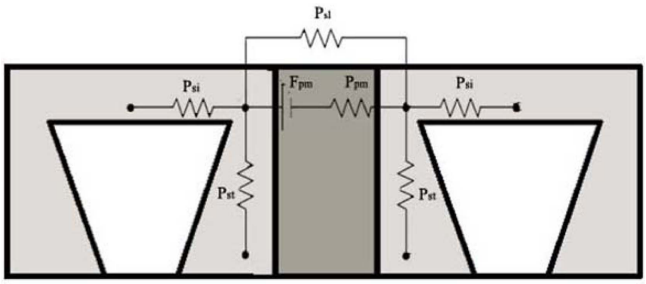

(a)

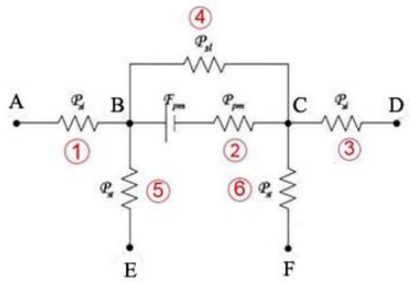

(b)

Fig. 4. (Color online) Stator Magnetic Equivalent Circuit module: (a) stator section; (b) MEC of stator section.

2.1.1.2. Stator MEC Modules

MEC model of magnetic flux distribution between central axes of two neighboring stator windings (i.e. unit section of stator) is defined as stator MEC module. Fig. 4(a) represents unit section of stator, and corresponding magnetic equivalent circuit module is shown in Fig. 4(b). Branches and nodes of circuit are represented by numbers and alphabets, respectively. As PM is situated in stator, permeance in series with mmf source is used for its representation. Flux paths in the stator back iron and stator tooth results in different types flux tubes with permeances P_{si} and P_{st}, respectively. Leakage flux is also included in stator MEC module and modeled as permeance P_{sl}, as shown in Fig. 4(a). Table 3 represents information about structure of flux tubes (illustrated in Fig. 3) observed from FEA simulations for permeance calculations.

Table 3. Types of flux tubes observed from FEA simulations in stator and rotor magnetic equivalent circuit modules.

Point of observation	Type of flux tube
P_{rt}	b
P_{ri}	a
P_{si}	b
P_{sl}	e
P_{pm}	b
P_{st}	a

Reluctance network of 12/10 SFPMM's stator is established by merging twelve similar stator magnetic equivalent circuit modules as shown in Fig. 4(b) with a modification of mmf source polarity. As branch BC of Fig. 4(b) shows mmf source with permeance in series, its polarity should be reversed in every alternate module. Variation of magnetic flux paths in stator with change in rotor position is neglected.

2.1.1.3. Rotor MEC Modules

MEC model representing magnetic flux distribution in a unit section of rotor is defined as rotor MEC module. For this purpose, rotor of SFPMM is divided into ten equal sections with rotor tooth in the middle of each section. Fig. 5(a) represents unit section of rotor, and corresponding magnetic equivalent circuit module is shown in Fig. 5(b). Branches and nodes of circuit are represented by numbers and alphabets, respectively. Flux paths in the rotor back iron and rotor tooth results in different types flux tubes with permeances P_{ri} and P_{rt}, respectively. Table 3 represents information about structure of flux tubes (illustrated in Fig. 3) observed from FEA simulations for permeance calculation.

Reluctance network of 12/10 SFPMM's rotor is established by merging ten similar rotor magnetic equivalent circuit modules as shown in Fig. 5(b). Rotor MEC modules are also assumed to be invariant to the rotor position.

2.1.1.4. Air-gap MEC Modules

Flux distribution of air-gap area surrounding rotor tooth is represented by Magnetic Equivalent Circuit model and

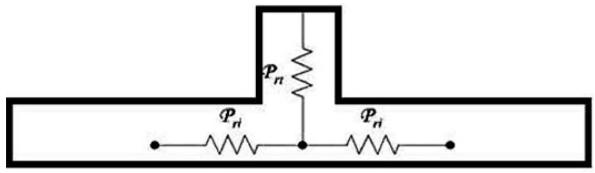

(a)

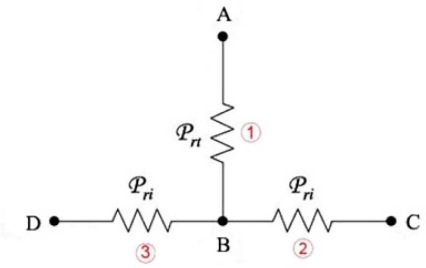

(b)

Fig. 5. (Color online) Rotor Magnetic Equivalent Circuit module: (a) rotor section; (b) MEC of rotor section.

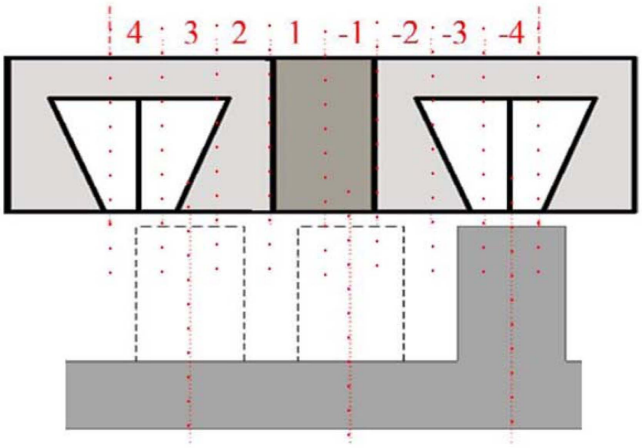

Fig. 6. (Color online) Different stator segments corresponding to rotor tooth position.

is termed as air-gap MEC module. As air-gap MEC modules are sensitive to rotor position, different air-gap magnetic equivalent circuit modules are modeled corresponding to different rotor positions. To avoid computational complexity, stator of 12/10 SFPMM is divided into eight segments (Fig. 6). As rotor tooth enters different stator's segment, different air-gap magnetic equivalent circuit module is used. PM is selected as central axis of stator, four segments on the right side, numbered from –1 to –4, are symmetric to four segments on the left side, numbered from 1 to 4, thus to model whole air-gap magnetic equivalent circuit only four air-gap magnetic equivalent circuit modules are required.

FEA of 12/10 SFPMM is performed to model air-gap magnetic flux distribution when rotor tooth travels in different segments, as shown in Fig. 7. Flux tubes for air-gap flux distribution obtained from FEA are shown in Fig. 8(a) (Segment 1), Fig. 9(a) (Segment 2), Fig. 10(a)

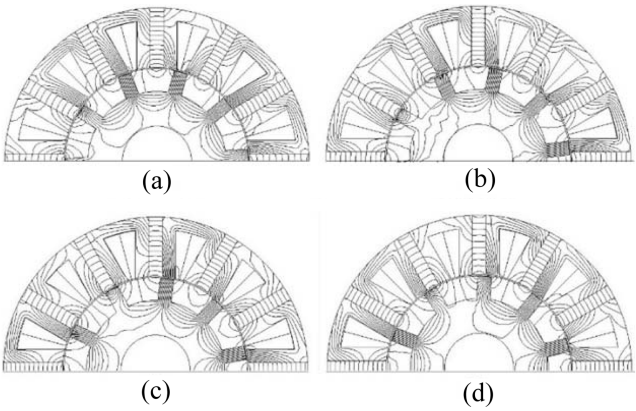

Fig. 7. FEA results of 12/10 PMFSM while rotor tooth travel in (a) Segment 1, (b) Segment 2, (c) Segment 3, (d) Segment 4.

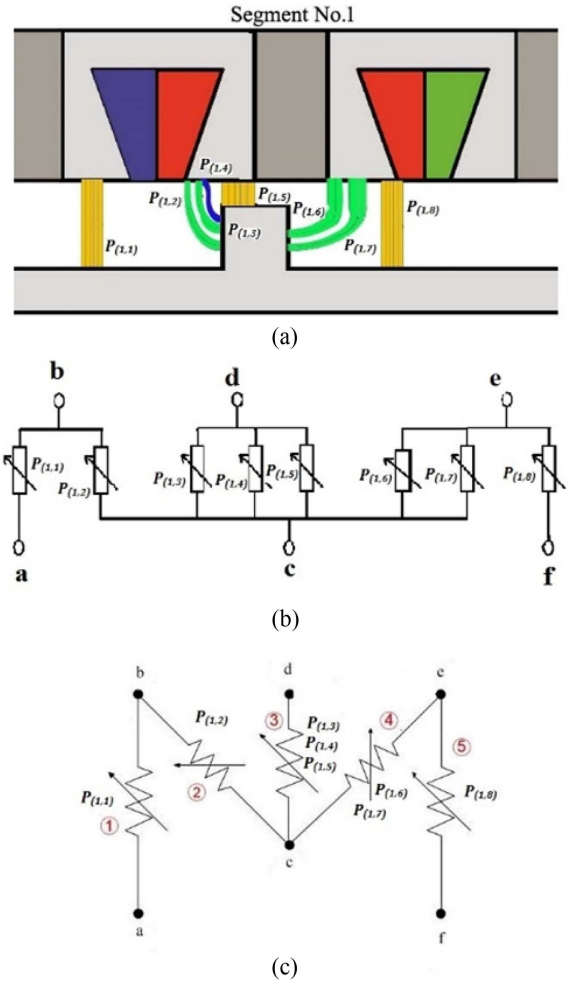

Fig. 8. (Color online) Air-gap Magnetic Equivalent Circuit Module 1; (a) Air-gap flux tubes corresponding to rotor tooth for Segment No. 1, (b) Detailed MEC, and (c) Air-gap MEC topology.

(Segment 3), and Fig. 11(a) (Segment 4). Table 4 illustrates types of flux tubes (shown in Fig. 3) observed from FEA simulations for permeance calculations. Permeance calculation for each flux tube is done by using equations introduced in Table 2. Four different air-gap magnetic equivalent circuit modules with variable permeances are shown in Fig. 8(b) (Segment 1), Fig. 9(b) (Segment 2), Fig. 10(b) (Segment 3), and Fig. 11(b) (Segment 4). Multiple parallel permeances are reduced to single branch permeance and four different topologies are presented in Fig. 8(c) (Segment 1), Fig. 9(c) (Segment 2), Fig. 10(c) (Segment 3), and Fig. 11(c) (Segment 4).

2.1.2. Solution methodology

Five rotor magnetic equivalent circuit modules, six stator magnetic equivalent circuit modules, and five air-gap magnetic equivalent circuit modules numbered as T1-

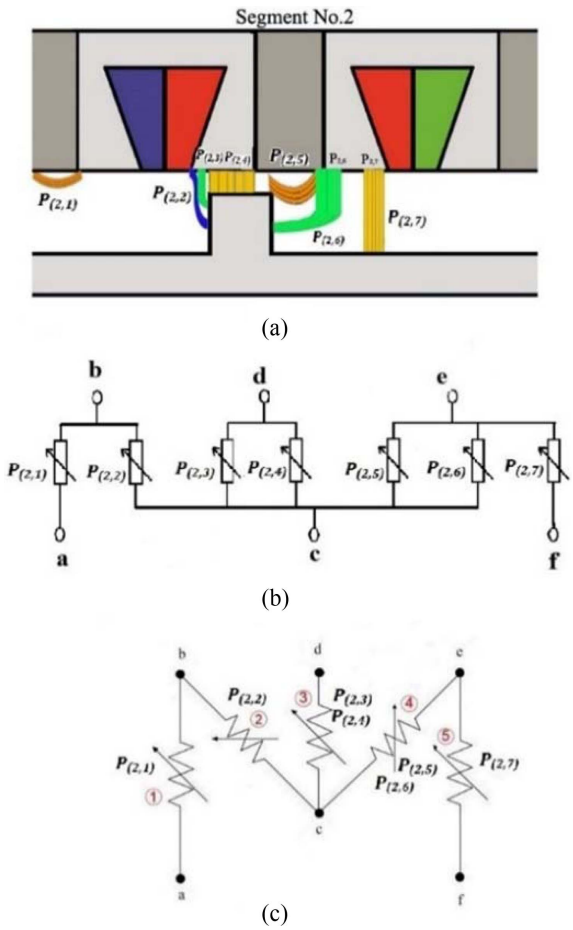

Fig. 9. (Color online) Air-gap Magnetic Equivalent Circuit Module 2; (a) Air-gap flux tubes corresponding to rotor tooth for Segment No. 2, (b) Detailed MEC, and (c) Air-gap MEC topology.

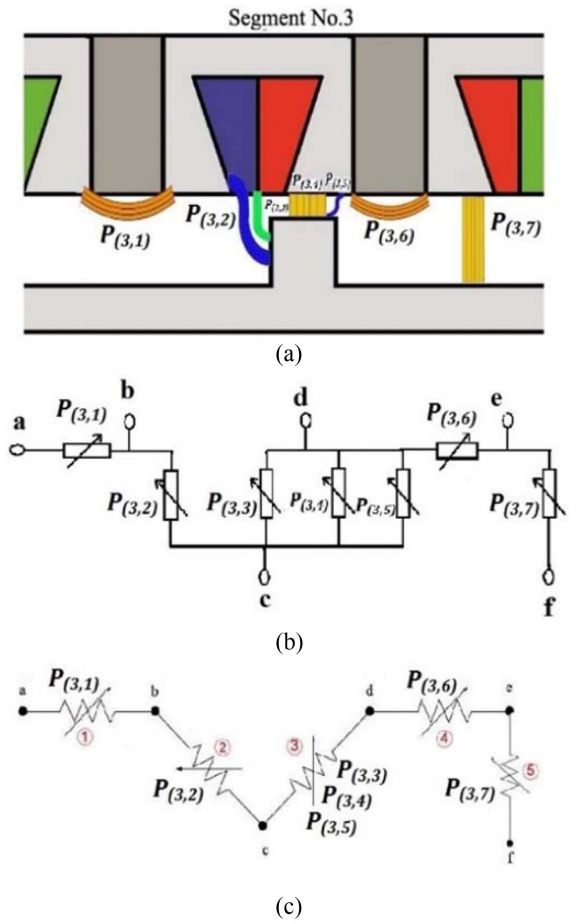

Fig. 10. (Color online) Air-gap Magnetic Equivalent Circuit Module 3; (a) Air-gap flux tubes corresponding to rotor tooth for Segment No. 3, (b) Detailed MEC, and (c) Air-gap MEC topology.

T5, S1-S6, and A1-A5, respectively are used to model SFPMM due to its periodic nature as shown in Fig. 12.

Air-gap MEC modules are sensitive to rotor tooth position and results in different reluctance network topologies corresponding to change in rotor position. Sequence of air-gap magnetic equivalent circuit modules types for every rotor position is established and is termed as shifting scheme of rotor position states. Shift of rotor position states can be mathematically predicted due to fact that rotor position states are an array of segment numbers of rotor teeth. Shifting scheme for 12/10 SFPMM position states is presented in Table 5. Ten rotor teeth (T1-T10) are represented in columns, eight position states (S1-S8) are presented in rows and the number represents the travelling segment of each rotor tooth.

Magnetic potentials of each node are computed by describing MEC modules mathematically as matrices, these matrices are merged to form GRN and solved using incidence matrix method [37] utilizing MATLAB Software. Main features of incidence matrix method are explained as follows.

Incidence matrix A of a circuit having m nodes and n branches is $m \times n$ matrix, in which

$$A_{x,y} = \begin{cases} 0, & \text{when branch } y \text{ is not connected to node } x, \\ -1, & \text{when branch } y \text{ ends to node } x, \\ 1, & \text{when branch } y \text{ begins from node } x. \end{cases} \tag{5}$$

Following equations are derived according to Kirchhoff Circuit Laws:

$$U = \boldsymbol{A}^t . V \tag{6}$$

Where, U is the mmf drop across each branch and is $n \times 1$ vector, A is incidence matrix of $m \times n$ dimensions, and V is magnetic potential on each node ($m \times 1$ vector).

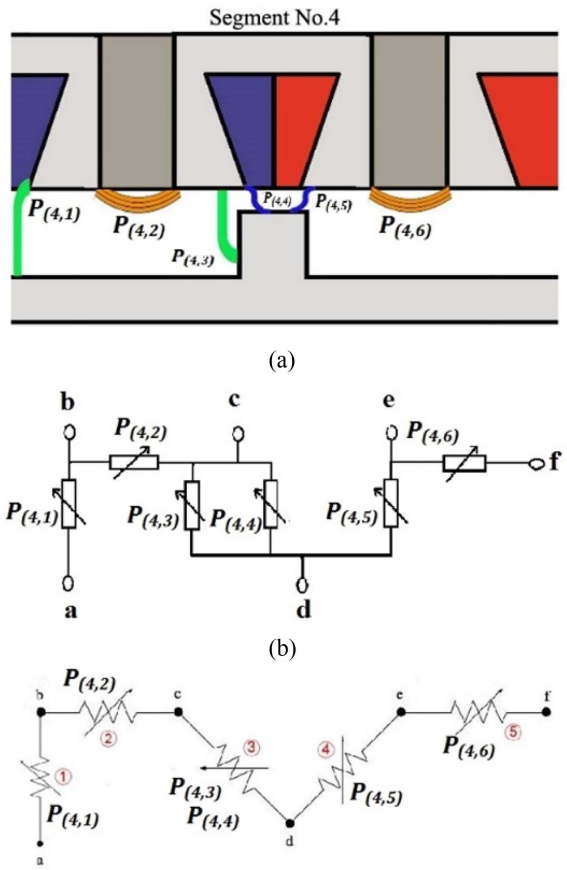

Fig. 11. (Color online) Air-gap Magnetic Equivalent Circuit Module 4; (a) Air-gap flux tubes corresponding to rotor tooth for Segment No. 4, (b) Detailed MEC, and (c) Air-gap MEC topology.

Table 4. Types of flux tubes tubes observed from FEA simulations in different air-gap MEC modules.

Flux tube Number	Segment Number			
	Segment 1	Segment 2	Segment 3	Segment 4
1	c	e	e	d
2	d	f	f	e
3	d	d	d	d
4	f	c	c	f
5	c	e	f	f
6	d	d	e	e
7	d	c	c	-
8	c	-	-	-

$$\boldsymbol{A}.\Phi = 0 \tag{7}$$

Where, Φ is the flux through each branch and is $n \times 1$ vector.

$$U = \boldsymbol{R}.\Phi + E = \Lambda^{-1}.\Phi + E \tag{8}$$

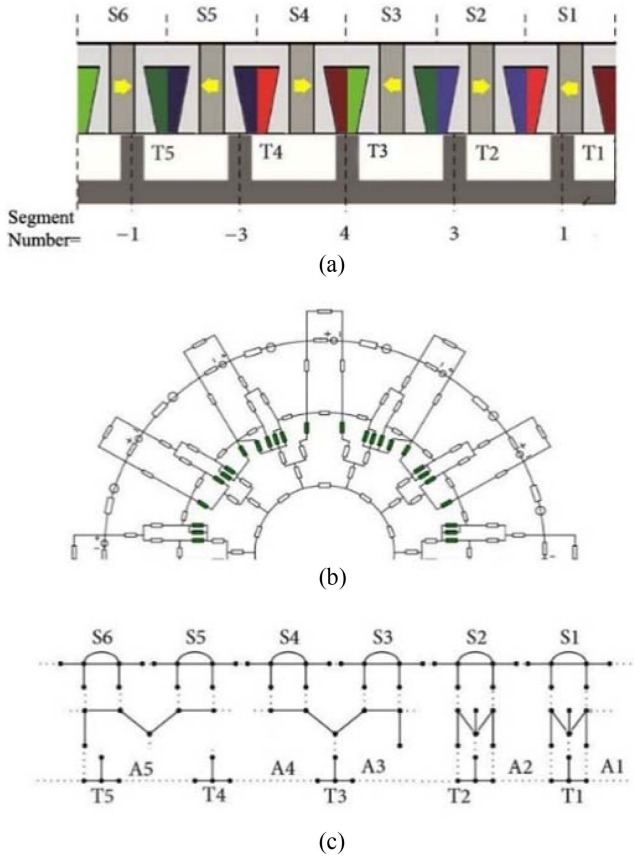

Fig. 12. (Color online) Complete GRN for half of 12/10 SFPMM: (a) cross-section in polar coordinates, (b) combined MEC model of stator, rotor and different air-gaps, (c) network topology.

Where, R is $n \times n$ diagonal matrix representing reluctance of each branch, E is mmf source in each branch ($n \times 1$ vector), and Λ is $n \times n$ diagonal matrix representing permeance of each branch. Equation for magnetic potential (utilizing A, Λ, and E) can be written as;

$$V = (\boldsymbol{A}.\Lambda.\boldsymbol{A}^{t})^{-1}.\ (\boldsymbol{A}.\Lambda.E) \tag{9}$$

Magnetic potentials of each node are calculated by using Equation (9) that ultimately helps to compute magnetic flux through each flux tube.

2.2. Analytical prediction of cogging torque

Cogging torque is introduced due to interaction of PMs and armature winding, and may affect control strategy. Structure of SFPMM rotor shows resemblance with SRM i.e. double salient in nature, this property reveals an inherent disadvantage of significant cogging force. An appropriate design of SFPMM must suppress cogging torque, as it has significant value even in case of light or no-load condition. Cogging torque can be reduced by: (a)

Table 5. Change in rotor position state during rotation.

	S1	S2	S3	S4	S5	S6	S7	S8			
T1	-4	-4	-1	1	-4	-4	-1	1	-3	-2	1
T2	-3	-2	1	2	-3	-2	1	2	-1	1	3
T3	-1	1	3	4	-1	1	3	4	-3	2	4
T4	-3	2	4	-3	-3	2	4	-3	-4	4	-3
T5	-4	3	-3	4	-4	4	-3	4	-4	-4	-1
T6	-4	-4	-1	1	-4	-4	-1	1	-3	-2	-1
T7	-3	-2	1	2	-3	-2	1	2	-1	1	3
T8	-1	1	3	4	-1	1	3	4	-3	2	4
T9	-3	2	4	-3	-3	2	4	-3	-4	4	-3
T10	-4	4	-3	4	-4	4	-3	4	-4	-4	-1

narrow manufacturing tolerances, (b) rotor skewing techniques, (c) pole shaping, (d) rotor teeth notching, (e) rotor teeth axial pairing, and (f) flanging techniques. However, average torque production is reduced by applying aforementioned techniques [38].

Objective of this section is to develop accurate and convenient analytical tool for analysis of cogging torque. Energy method and FA technique of air-gap flux density and air-gap permeance is implemented to predict cogging torque of SFPMM. Cogging torque for traditional PM machines is defined in literature [39-41]. Consequently, cogging force for SFPMM can be defined as no-load torque without armature winding excitation, and can be expressed as:

$$T_\alpha = \frac{\partial W_{ft}}{\partial \alpha} \tag{10}$$

$$T_\alpha = -\frac{\partial (W_{gap} + W_{PM})}{\partial \alpha} \tag{11}$$

$$T_\alpha \approx \frac{\partial W_{gap}}{\partial \alpha} \tag{12}$$

Where W_{ft}, W_{gap}, and W_{PM} are magnetic energies of machine, air-gap and magnets, respectively. Whereas α is a variable representing rotor movement.

$$W_{gap} = \frac{1}{2\mu_0}\int B_\delta^2(\theta)dV \tag{13}$$

$$B_\delta^2 = B_r^2(\theta).\left(\frac{L(\theta)}{L(\theta)+\delta_{(\theta,\alpha)}}\right) \tag{14}$$

Where θ is the angle along the circumference of air gap,

$$W_{gap} = \frac{1}{2\mu_0}\int B_r^2(\theta).\left(\frac{L(\theta)}{L(\theta)+\delta_{(\theta,\alpha)}}\right)^2 dV \tag{15}$$

The Fourier expansions of $B_r^2(\theta)$ and $\frac{L(\theta)}{L(\theta)+\delta_{(\theta,\alpha)}}$ can be derived as

$$B_r^2(\theta) = B_{r0} + \sum_{n=1}^{\infty} B_{rn}\cos N_s n\theta \tag{16}$$

$$B_{r0} = \frac{\beta_s B_r^2}{\tau_s} \tag{17}$$

$$B_{rn} = \frac{2}{n\pi}B_r^2\sin\left(\frac{nB_s\pi}{\tau_s}\right) \tag{18}$$

Thus we have

$$B_r^2(\theta) = \frac{\beta_s B_r^2}{\tau_s} + \sum_{n=1}^{\infty}\frac{2}{n\pi}B_r^2\sin\left(\frac{nB_s\pi}{\tau_s}\right)\cos N_s n\theta \tag{19}$$

$$B_r^2(\theta) = \frac{\beta_s B_r^2}{\tau_s} + \frac{2}{n\pi}B_r^2\sum_{n=1}^{\infty}\sin\left(\frac{nB_s\pi}{\tau_s}\right)\cos N_s n\theta \tag{20}$$

Where β_s, τ_s, and N_s is stator pole arc width, pole pitch of stator, and stator pole number, respectively. Whereas B_r is residual flux density of PM.

$$\left(\frac{L(\theta)}{L(\theta)+\delta_{(\theta,\alpha)}}\right)^2 = G_o + \sum_{m=1}^{\infty} G_m\cos mN_r(\theta+\alpha) \tag{21}$$

$$\left(\frac{L(\theta)}{L(\theta)+\delta_{(\theta,\alpha)}}\right)^2 = G^2(\theta) \tag{22}$$

$$G^2(\theta) = G_o + \sum_{n=1}^{\infty} G_{nN_s}\cos nN_s\theta d\theta \tag{23}$$

$$G_o = \frac{N_a a}{2\pi}\left(\frac{L}{L+\delta}\right)^2 \tag{24}$$

$$G_{nN_s} = \frac{2}{n\pi}\left(\frac{L}{L+\delta}\right)^2(-1)^n\sin\left(\frac{nN_s a}{2}\right) \tag{25}$$

Thus we have,

$$G^2(\theta)=\frac{N_s a}{2\pi}\left(\frac{L}{L+\delta}\right)^2+\sum_{n=1}^{\infty}\frac{2}{n\pi}\left(\frac{L}{L+\delta}\right)^2(-1)^n\sin\left(\frac{nN_s a}{2}\right)\cos nN_s\theta d\theta \tag{26}$$

$$G^2(\theta)=\frac{N_s a}{2\pi}\left(\frac{L}{L+\delta}\right)^2+\frac{2}{n\pi}\left(\frac{L}{L+\delta}\right)^2\sum_{n=1}^{\infty}(-1)^n\sin\left(\frac{nN_s a}{2}\right)\cos nN_s\theta d\theta \tag{27}$$

Solving for W_{gap}, we have

$$W_{gpa}=\frac{1}{2\mu_o}\int\left(\frac{\beta_2 B_r^2}{\tau_s}+\frac{2}{n\pi}B_r^2\sum_{n=1}^{\infty}\sin\left(\frac{nB_s\pi}{\tau_s}\right)\cos N_s n\theta\right).\left(\frac{N_s a}{2\pi}\left(\frac{L}{L+\delta}\right)^2+\frac{2}{n\pi}\left(\frac{L}{L+\delta}\right)^2\sum_{n=1}^{\infty}(-1)^n\sin\left(\frac{nN_s a}{2}\right)\cos nN_s\theta d\theta\right)dV \tag{28}$$

Where N_r is the rotor pole number, G_m the Fourier coefficients. The analytical expression can be deduced as

$$T_{cog}(\alpha)=\frac{\pi N_r L}{4\mu_o}(R_2^2-R_1^2)\sum_{m=1}^{\infty}nG_m B_{\frac{nN_r}{N_s}}\sin nN_r\alpha \tag{29}$$

Where L is the stack length, R_1 is the radius of outer rotor, R_2 is radius of inner stator, and μ_o the permeability of the air.

2.3. Analytical prediction of electromagnetic torque

Electromagnetic toque is the overall torque developed due to mutual effect of PMs and armature winding current. Literature survey reveals that relative air-gap permeance (MEC) model can predict radial component of magnetic field with good accuracy [19], this type of model is acceptable for no-load operation. Prediction of electromagnetic torque require accurate information of both radial and tangential components of flux density. Here, FA plays an important role by providing sophisticated analytical expression for both radial and tangential components [19]. Aforementioned components of flux density are combined by MST method, are can be represented as;

$$T=\frac{1}{\mu_o}L_a\int_0^{2\pi}B_{sr}(r,\theta,\alpha)B_{s\theta}(r,\theta,\alpha)d\theta \tag{30}$$

Where L_α is the stack length and μ_o is permeability of free space/vacuum.

Flux density in air-gap of PM machines can be written as,

$$B_s(r,\theta,\alpha)=[B_r(r,\theta,\alpha)+jB_\theta(r,\theta,\alpha)].[\lambda_a(r,\theta)-j\lambda_b(r,\theta)] \tag{31}$$

$$B_s(r,\theta,\alpha)=B_{sr}(r,\theta,\alpha)+jB_{s\theta}(r,\theta,\alpha) \tag{32}$$

B_{sr} and $B_{s\theta}$ in term of complex relative air-gap permeance can be written as [42, 43];

$$B_{sr}=R_e(B_k\lambda^*)=B_r\lambda_a+B_\theta\lambda_b \tag{33}$$

$$B_{s\theta}=I_m(B_k\lambda^*)=B_\theta\lambda_a-B_r\lambda_b \tag{34}$$

Where B_r and B_θ are the radial and tangential components of the flux density in air-gap, and λ^* represents the complex conjugate of complex relative air-gap permeance with λ_a and λ_b as its real and imaginary part, respectively.

The distribution of flux density and complex permeance along a circular arc inside the air-gap can be written as in the form of Fourier series;

$$B_r(r,\theta,\alpha)\sum_n B_{rn}(r)\cos[np(\theta-\alpha)] \tag{35}$$

$$B_\theta(r,\theta,\alpha)\sum_n B_{\theta n}(r)\sin[np(\theta-\alpha)] \tag{36}$$

Fourier coefficients B_{rn} and $B_{\theta n}$ are calculated from [44],

$$B_{rn}(r)=\sum_{n=1,3,5,\ldots}^{\infty}\frac{B_r 4}{\mu_r n\pi}\sin\left(\frac{n\pi\alpha_p}{2}\right)\frac{np}{(np)^2-1}\left[\left(\frac{r}{R_s}\right)^{np-1}\left(\frac{R_m}{R_s}\right)^{np+1}+\left(\frac{R_m}{r}\right)^{np+1}\right].\left\{\frac{np-1+2\left(\frac{R_r}{R_m}\right)^{np+1}-(np+1)\left(\frac{R_r}{R_m}\right)^{2np}}{\frac{\mu_r+1}{\mu_r}\left[1-\left(\frac{R_r}{R_s}\right)^{2np}\right]-\frac{\mu_r-1}{\mu_r}\left[\left(\frac{R_m}{R_s}\right)^{2np}-\left(\frac{R_m}{R_s}\right)^{2np}\right]}\right\} \tag{37}$$

And,

$$B_{\theta n}(r)=\sum_{n=1,3,5,\ldots}^{\infty}\frac{B_r 4}{\mu_r n\pi}\sin\left(\frac{n\pi\alpha_p}{2}\right)\frac{np}{(np)^2-1}\left[-\left(\frac{r}{R_s}\right)^{np-1}\left(\frac{R_m}{R_s}\right)^{np+1}+\left(\frac{R_m}{r}\right)^{np+1}\right].\left\{\frac{np-1+2\left(\frac{R_r}{R_m}\right)^{np+1}-(np+1)\left(\frac{R_r}{R_m}\right)^{2np}}{\frac{\mu_r+1}{\mu_r}\left[1-\left(\frac{R_r}{R_s}\right)^{2np}\right]-\frac{\mu_r-1}{\mu_r}\left[\left(\frac{R_m}{R_s}\right)^{2np}-\left(\frac{R_r}{R_m}\right)^{2np}\right]}\right\} \tag{38}$$

Where B_r is the magnet remanence, μ_r is the relative recoil permeability, α_p is the magnet-arc to pole-pitch ratio, R_m is the radius at the magnet surface, R_s is the radius at the stator inner surface, R_r and is the radius at the rotor core outer surface.

Complex relative air-gap permeance can be written as [43],

Fig. 13. (Color online) Real component of complex relative air-gap permeance.

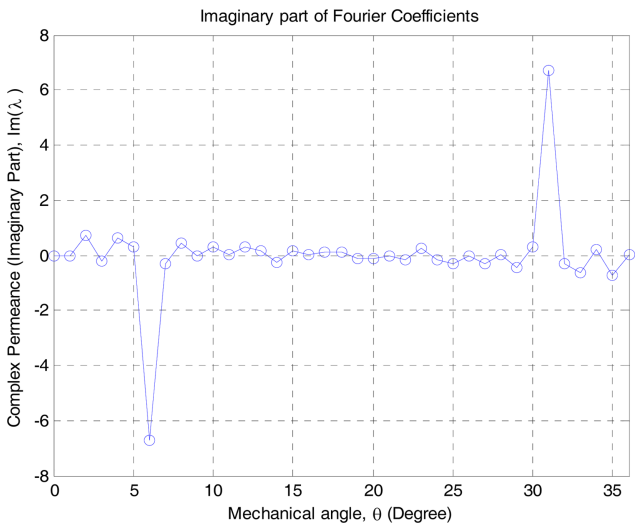

Fig. 14. (Color online) Imaginary component of complex relative air-gap permeance.

$$\lambda = \lambda_a + j\lambda_b \tag{39}$$

Waveforms of real and imaginary parts of complex relative air-gap permeance are shown as in Fig. 13 and Fig. 14, respectively.

These waveforms can be expressed as in the form of Fourier series to define complex permeance function of entire air-gap, i.e.

$$\lambda_a = \lambda_o + \sum_{n=1}^{N_\lambda} \lambda_{an} \cos(nQ_s\theta) \tag{40}$$

$$\lambda_b = \sum_{n=1}^{N_\lambda} \lambda_{bn} \sin(nQ_s\theta) \tag{41}$$

Where Q_s is the number of slots and N_λ is the maximum order of the Fourier coefficients. The Fourier coefficients λ_{an} and λ_{bn} are calculated using waveforms shown in Fig. 13 and Fig. 14 utilizing Discrete Fourier Transform (DFT) methodology.

3. Validation of Analytical Prediction with FEA

Analytical calculations for three fundamental parameters namely, (a) open-circuit flux linkage (utilizing MEC with GRN methodology), (b) cogging torque (utilizing FA), and (c) electromagnetic torque (utilizing MST method) of proposed twelve-stator-slot and ten-rotor-tooth (12/10) with trapezoidal slot structure SFPMM corresponding to different rotor positions are validated by comparing results with corresponding universally accepted FEA results. Thanks to accuracy of developed method, authors are confident to recommend developed method for initial design and sizing of SFPMM.

3.1. Validation of analytical prediction for open-circuit flux linkage

Accuracy of nonlinear magnetic equivalent circuit models with GRN methodology for 12/10 SFPMM is validated by comparing open-circuit phase flux linkage with corresponding FEA results. Comparison of open-circuit phase flux linkage obtained by utilizing MEC with GRN methodology and FEA is presented in Fig. 15. Error of open-circuit phase flux linkage between MEC with GRN methodology and FEA results is also computed and shown in Fig. 16. Comparison of results shows errors less

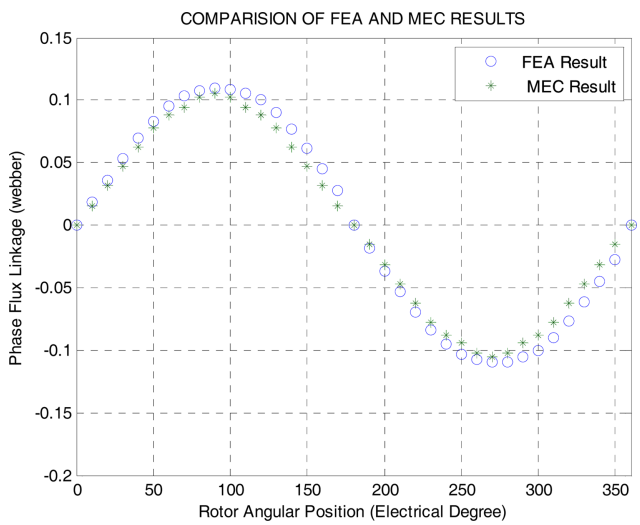

Fig. 15. (Color online) Comparison of open-circuit phase flux linkage obtained by utilizing MEC with GRN methodology and FEA.

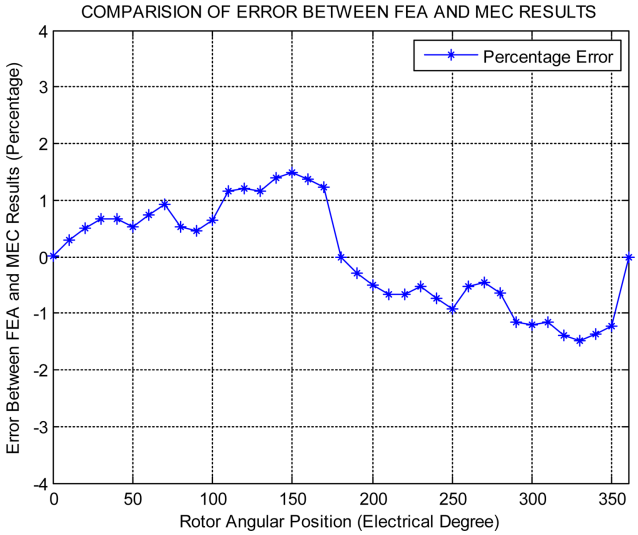

Fig. 16. (Color online) Error of open-circuit phase flux linkage between MEC with GRN methodology and FEA.

than ~2%, hence validating accuracy of MEC with GRN methodology.

3.2. Validation of analytical prediction for cogging torque

Results obtained for 12/10 SFPMM by analytical modelling (Equation 29) is validated by comparing with corresponding FEA results. Comparison of cogging torque obtained by FA and FEA is shown in Fig. 17. Moreover, point to point error is also calculated (shown in Fig. 18) and errors are less than ~4.2%, hence validating accuracy of FA.

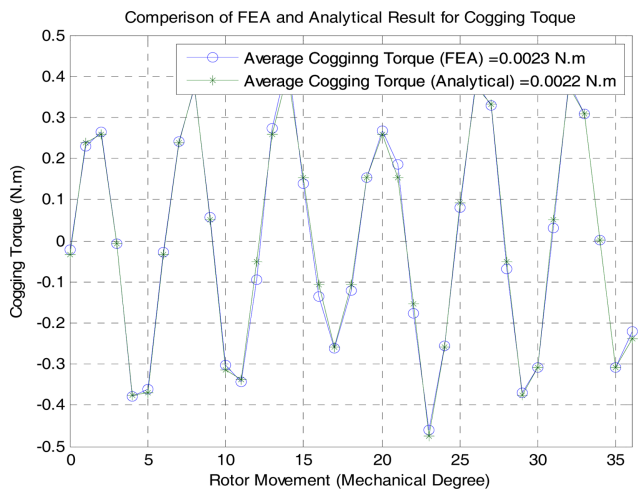

Fig. 17. (Color online) Comparison of Cogging Torque obtained by FA and FEA.

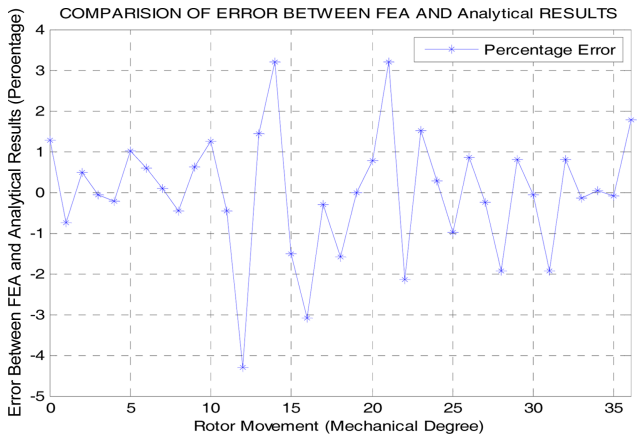

Fig. 18. (Color online) Point-to-point error of cogging torque obtained by FA and FEA.

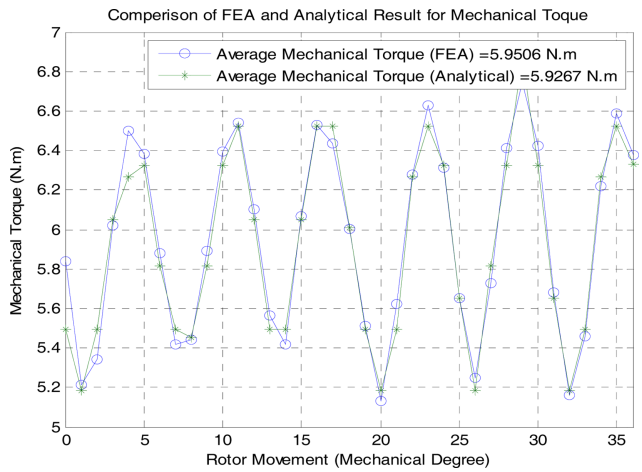

Fig. 19. (Color online) Comparison of electromagnetic torque obtained by MST method and FEA.

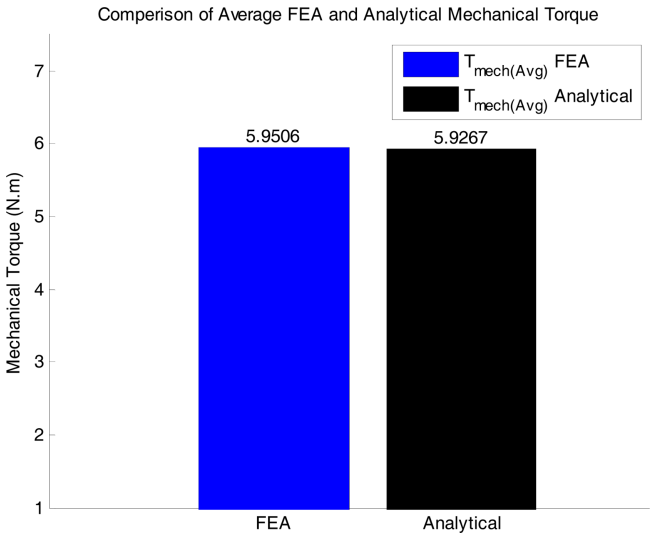

Fig. 20. (Color online) Comparison of average torque values obtained by MST method and FEA.

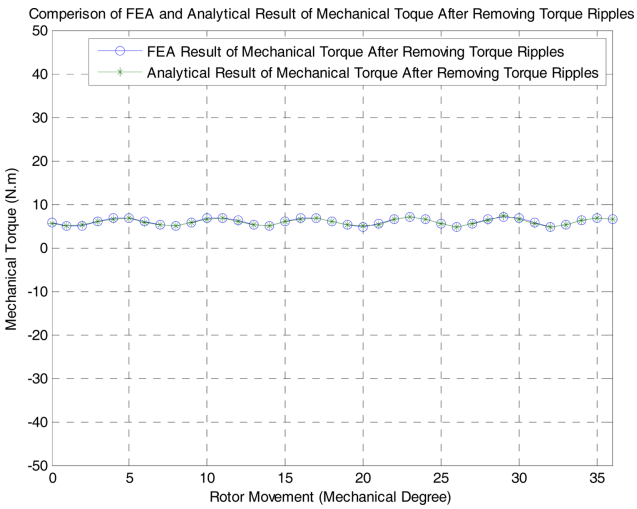

Fig. 21. (Color online) Output torque of SFPMM.

3.3. Validation of analytical prediction for electromagnetic toque

Comparison of analytical predicted results for electromagnetic torque obtained for 12/10 SFPMM by Maxwell Stress Tensor Method (Equation 30) and FEA is shown in Fig. 19. Thanks to accuracy of developed method, results obtained by MST method fairly match corresponding FEA results. Moreover, average torque is also calculated using MST method and compared with corresponding FEA results, and reveals errors less than ~2% (as shown in Fig. 20).

Electromechanical torque includes both output torque and cogging torque [45]. Output torque (viz. values after subtraction of cogging torque from electromagnetic torque) for both MST and FEA is calculated and compared, as shown in Fig. 21. Output torque still shows torque ripples, possible reasons to knowledge of authors are assumptions described in Section 2.

4. Conclusions

Switched Flux Permanent Magnet Machines (PMFSM) attracted interest of researchers due to its high revolution per second (RPS) withstand property, robust rotor structure, high torque capability, high power density, and its compatibility with extreme environmental conditions. Thanks to accuracy of developed method, authors are confident to recommend developed method for initial design and sizing of SFPMM.

In this paper, magnetic equivalent circuit (MEC) for stator, rotor, and air-gap (corresponding to different rotor positions) of proposed twelve-stator-slot and ten-rotor-tooth (12/10) with trapezoidal slot structure SFPMM are defined. These MEC models are combined as Global Reluctance Network (GRN) and are solved utilizing incidence matrix methodology. Accuracy of nonlinear magnetic equivalent circuit models and GRN methodology for 12/10 SFPMM is validated by comparing open-circuit phase flux linkage with corresponding FEA results, and shows less than ~2% error. Furthermore, energy method and FA technique of air-gap flux density and air-gap permeance is implemented to predict cogging torque. Moreover, MST method is integrated for prediction of electromagnetic torque by utilizing analytical expressions of both radial and tangential component of magnetic field. Analytical predictions for cogging torque and average electromagnetic torque shows errors less than ~4.2% and ~2% to corresponding FEA results, respectively.

References

[1] E. Hoang, A. H. Ben-Ahmed, and J. Lucidarme, Conference Record of the 7th European Conference on Power Electronics and Application 1997, **3**, 903 (1997).
[2] G. Henneberger and I. A. Viorel, Variable reluctance electrical machines, Shaker Verlag, Aachen, Germany (2001).
[3] A. S. Thomas, Z. Q. Zhu, R. L. Owen, G. W. Jewell, and D. Howe, IEEE Trans. Ind. Appl. **45**, 1971 (2009).
[4] Y. Cheng, C. Pollock, and H. Pollock, Conference Record of the Fourtieth IAS Annual Meeting 2005, **3**, 2168 (2005).
[5] S. E. Rauch and L. J. Johnson, AIEE Trans. **74**, 1261 (1955).
[6] I. Boldea, C. Wang, and S. A. Nasar, EMPS **27**, 849 (1999).
[7] R. P. Deodhar, S. Andersson, I. Boldea, and T. J. E. Miller, Conference Record of IEEE-IAS Annual Meeting 786 (1996).
[8] B. Sarlioglu, Y. F. Zhao, and T. A. Lipo, Conference Record of IEEE-IAS Annual Meeting **1**, 9 (1994).
[9] Z. Q. Zhu and D. Howe, Proceedings of the IEEE **95**, 746 (2007).
[10] Z. Q. Zhu and J. T. Chen, IEEE Trans. Magn. **46**, 1447 (2010).
[11] Z. Q. Zhu, Y. Pang, D. Howe, S. Iwasaki, R. Deodhar, and A. Pride, IEEE Trans. Magn. **41**, 4277 (2005).
[12] A. S. Thomas, Z. Q. Zhu, and L. J. Wu, IEEE Trans. Ind. Appl. **48**, (2012).
[13] F. Khan, E. Sulaiman, and M. Z. Ahmad, Conference Record of IEEE-PEOCO, Langkawi, Malaysia (2014).
[14] C. Hwang, C. Chang, S. Hung, and C. Liu, IEEE Trans. Magn. **50**, (2014).
[15] F. Khan, E. Sulaiman, and M. Z. Ahmad, Turkish Journal of Electrical Engineering & Computer Sciences **25**, 950 (2017).

[16] J. T. Chen, Z. Q. Zhu, S. Iwasaki, and R. Deodhar, IEEE Energy Conversion Congress and Exposition (ECCE), Atlanta, GA, USA, (2010).
[17] F. Barrero and M. J. Duran, IEEE Trans. Ind. Electron. **63**, (2016).
[18] A. Tessarolo, IEEE Trans. Energy Convers. **27**, 895 (2012).
[19] B. L. J. Gysen, K. J. Meesen, J. J. H Paulides, et al., IEEE Trans. Magn. **46**, 1499 (2010).
[20] J. T. Chen and Z. Q. Zhu, IEEE Trans. Energy Convers. **25**, (2010).
[21] C. Pollock and M. Wallace, Conference record of IEEE-IAS Annual Meeting, **3**, 1980 (1999).
[22] C. Pollock, H. Pollock, R. Barron, et al., 38th IEEE-IAS Annual Meeting, Salt Lake City, USA, 2003.
[23] H. Pollock, C. Pollock, R. T. Walter, et al., 38th IEEE-IAS Annual Meeting, Salt Lake City, USA, 2003.
[24] J. Zhang, M. Cheng, Z. Chen, and W. Hua, IEEE Trans. Energy Convers. **24**, (2009).
[25] Y. Pang, Z. Q. Zhu, D. Howe, S. Iwasaki, R. Deodhar, and A. Pride, Proceeding of International Conference on Electrical Machines and Systems, Seoul, Korea, (2007).
[26] B. Gaussens, E. Hoang, O. delaBarrière, J. Saint-Michel, M. Lécrivain, and M. Gabsi, IEEE Trans. Magn. **48**, (2012).
[27] Y. Tang, J. J. H. Paulides, and E. A. Lomonova, Hindawi Publishing Corporation, ISRN Automotive Engineering, (2014).
[28] Y. Chen, Z. Q. Zhu, and D. Howe, IEEE Trans. Ind. Appl. **44**, (2008).
[29] D. Li, R. Qu, X. Zhang, and Y. Liu, IEEE-ECCE, Raleigh, NC, USA, (2012).
[30] D. Wang, X. Wang, and S. Jung, J. Magn. **18**, 361 (2013).
[31] Y. Tang, T. E. Motoasca, J. J. H. Paulides, and E. A. Lomonova, International Conference on Electrical Machines (ICEM), 2792 (2012).
[32] N. Ullah, F. Khan, W. Ullah, M. Umair, and Z. Khattak, Conference Record of IEEE-IBCAST, Islamabad, Pakistan, 2018.
[33] E. Ilhan, B. L. J. Gysen, J. J. H. Paulides, and E. A. Lomonova, IEEE Trans. Magn. **46**, 1762 (2010).
[34] A. Dwivedi, S. K. Singh, and R. K. Srivastava, IET Electr. Power Appl. **10**, 539, (2016).
[35] Le Besnerais, V. Lanfranchi, M. Hecquet, and P. Brochet, IEEE Trans. Magn. **45**, 3131 (2009).
[36] V. Ostovic, Dynamics of saturated electric machines, Berlin Heidelberg, Germany: Springer-Verlag New York Inc. (1989).
[37] L. O. Chuaand, P. M. Lin, Computer-Aided Analysis of Electronic Circuits-Algorithms and Computational Techniques, Prentice Hall, Englewood Cliffs, NJ, USA (1975).
[38] N. Fernando, I. U. Nutkani, S. Saha, and M. Naikinezhad, Proceedings of ICEMS (2017).
[39] X. Wang, Y. Yang, and D. Fu, J. Magn. Magn. Mater. **80**, 267 (2003).
[40] L. Zhu, S. Z. Jiang, Z. Q. Zhu, and C. C. Chan, IEEE Trans. Magn. **45**, 2023 (2009).
[41] D. Wang, X. Wang, D. Qiao, Y. Pei, and S.-Y. Jung, IEEE Trans. Magn. **47**, 2231 (2011).
[42] D. Zarko, D. Ban, and T. A. Lipo, IEEE Trans. Magn. **45**, 2943 (2009).
[43] D. Zarko, D. Ban, and T. A. Lipo, IEEE Trans. Magn. **44**, 52 (2008).
[44] Z. Q. Zhu, D. Howe, E. Bolte, and B. Ackermann, IEEE Trans. Magn. **29**, 124 (1993).
[45] L. Xue, L. Luo, Y. Gu, C. Chen, and Y. Li, Proceedings of ICEMS (2017).